SUPPLEMENTARY INFORMATION:

Weighing China's Fast Deployment of Offshore Wind Turbines through Satellite Images

Shujun Li[a], Peng Wang[a,b], Wen Li[c], Jiashuo Li[d], Nivedita Biyani[e], Weiqiang Chen[a,b]*

Author affiliations:

a. Key Lab of Urban Environment and Health, Institute of Urban Environment, Chinese Academy of Sciences, Xiamen, 361021, China

b. University of Chinese Academy of Sciences, Beijing, 100049, China

c. Department of Mechanical Engineering, The University of Melbourne, Building 170, Parkville, Victoria 3010, Australia

d. Institute of Blue and Green Development, Shandong University, Weihai, 264209, China.

e. Benioff Ocean Science Lab, University of California, Santa Barbara, California 93106, USA

**Corresponding author: Peng Wang (pwang@iue.ac.cn)*

Pages:30

Figures:24

Tables:7

Contents

S1 Methods

S1.1 Framework

Our framework consists of three critical procedures, which are outlined as follows:

(1) Offshore wind turbine data acquisition. Using integrated methodologies in Fig. S1.1 we collected fundamental empirical information for each offshore wind turbine, such as the turbine's geographic location, installation date, tower height, rotor diameter, offshore distance, capacity, and generator type. The acquisition of these spatial and measurement attributes serves multiple significant purposes. Firstly, the turbine's location and installation date are pivotal for tracking spatio-temporal installation trends associated with wind turbines[1]. Secondly, the tower height and rotor diameter play essential roles in determining the component's mass within wind turbines[2]. Additionally, offshore distance is closely linked to the length requirements of submarine cables[33]. Furthermore, capacity serves as a vital indicator of wind energy installation[4]. Finally, the generator type has a direct bearing on the weight of materials utilized in each wind turbine[5]. Thus, the selection of these attributes was driven by their collective capacity to provide a comprehensive overview of the mass and materials embedded within each wind turbine, enabling a nuanced analysis of offshore wind energy.

(2) In-use stock quantification. In our study, we harnessed machine learning to establish a robust connection between the gathered information mentioned above and the material percentages/intensities within each component of offshore wind turbines. As a result, we were able to quantify the in-use stock of key components (e.g. rotors and nacelles) and their associated raw materials (e.g. copper and aluminum) for each wind turbine across each year. Notably, we focused on four critical components: rotor, nacelle, tower, and submarine cable, all of which contribute significantly to the overall wind turbine material composition. For material quantification, we considered ten distinct categories of raw materials, encompassing seven bulk raw materials (low alloyed steel, high alloyed steel, cast iron, aluminum, copper, electrics/electronics, and other materials) and three rare earth elements (neodymium, dysprosium, and praseodymium). It's essential to point out that, foundations were excluded in this study, despite their contribution to the material mass of wind turbines. Our focus remained on the Wind Turbine Generator (defined as the composite entity comprising the tower, rotor,

and nacelle[6]) since it is installed and dismantled independently of the foundation[7]. Additionally, it's important to note that within our analysis, in-use stock analysis of blades and hubs was not further differentiated, which was collectively included within that of rotors.

(3) Spatiotemporal analysis. Our study delved into the spatiotemporal patterns of in-use stocks for components and materials within offshore wind turbines in China (offshore wind turbines in Taiwan are excluded in this study), including forming spatial density maps to assist in unveiling the extent of material stock aggregation within a given unit space, which could facilitate the policymakers with the development of efficient recycling routes[8]. The primary objective was to quantify the mass and spatial distribution of these stocks as well as to draw implications regarding their development over time.

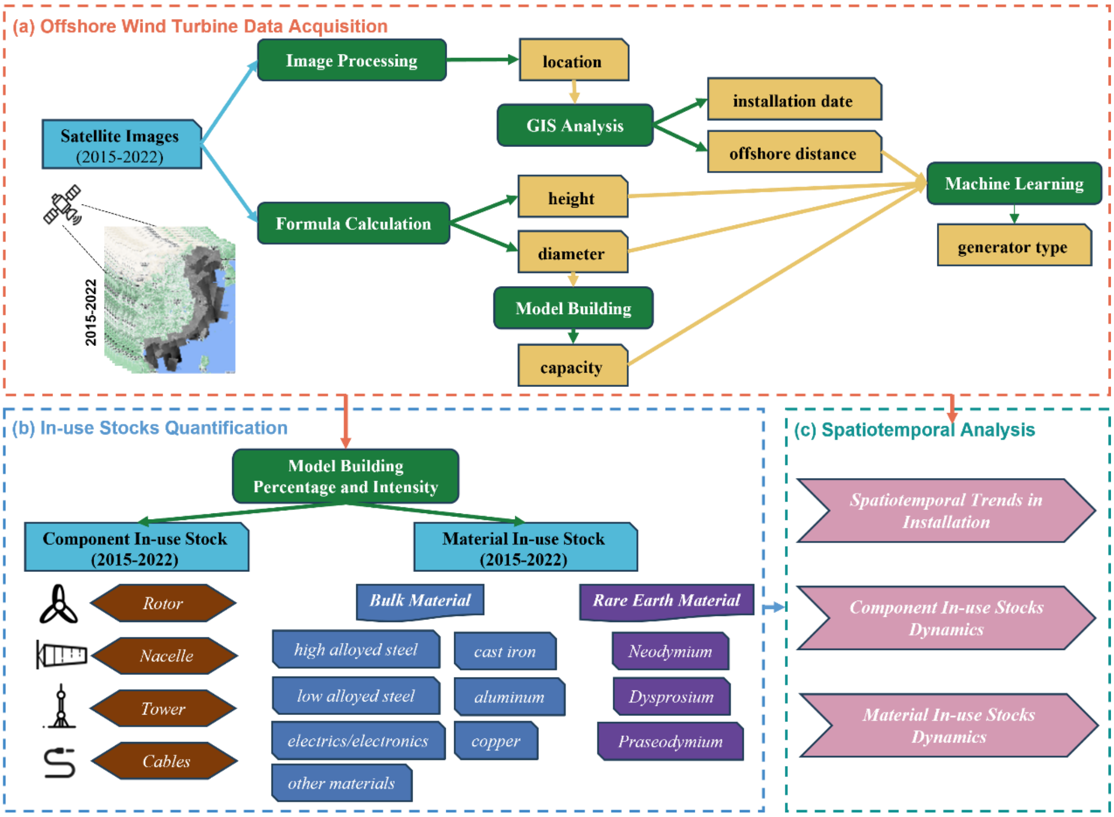

Fig. S1.1 Framework (a) Offshore wind turbine data acquisition process. (b) In-use stocks quantification content. (c) Spatiotemporal analysis list.

S1.2 Data sources

In this study, we utilized a multi-source data approach to gather information on offshore wind turbines in mainland China from 2015 to 2022. The following data sources were employed:

Earth observation data: We utilized Sentinel-1 satellite images with interferometric wide (IW) stripe mode and vertical (VV) polarization[9] to collect offshore wind turbine data.

Boundary shapefiles: To define the study area, we combined shapefiles representing land boundaries from OpenStreetMap(OSM)[10] and ocean areas within Exclusive Economic Zones (EEZ)[11].

Wind energy datasets: Open-source wind energy datasets, including the Danish Master Data Register of Wind Turbines (DMDRWT)[12], The Wind Power[13], 4C Offshore Wind Database[14] and Wind-turbine-models [15], were collected for model development and validation.

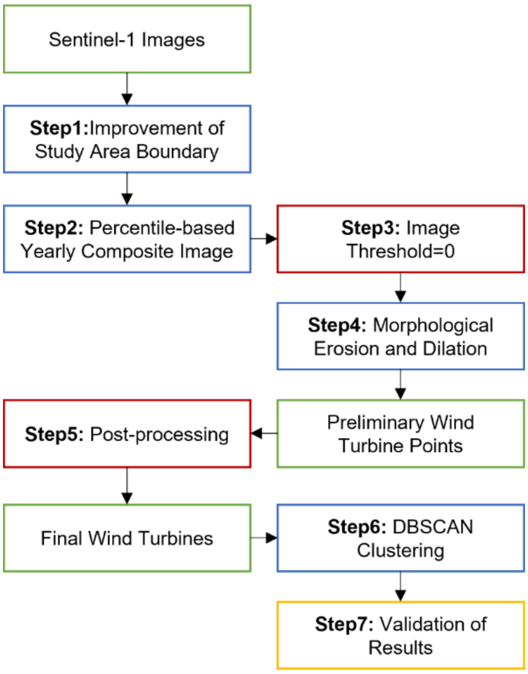

Fig. S1.2 Workflow of wind turbines extraction

S1.3 Offshore wind turbine screening

S1.3.1 Wind turbine location

The foundational approach is based on the methodology outlined in the literature[16], which includes two drawbacks: Firstly, features near the land-ocean interface, such as bridges and buildings, have the potential to be incorrectly identified as wind turbines. Secondly, the method's reliance on automatic thresholding can introduce instability, resulting in both the erroneous extraction and omission of offshore wind turbines. To address the gaps, we made three significant improvements, firstly, refinement of the study area boundary, and we modified the study area boundary based on data from OSM and EEZ. Secondly, threshold redefinition, we redefined the threshold for binary images depicting potential wind turbines. Lastly, post-processing, to obtain the final list of wind turbines, we implemented a post-processing step, which involved filtering and refining the results.

The wind turbine location extraction method employed in this study comprises six sequential steps (Fig. S1.2). In the **first step**, we redefined the study area boundaries using data from OSM and EEZ. The **second step** involves the elimination of floating or temporary objects using a percentile-based annual synthetic aperture radar (SAR) image acquisition reduction approach. The **third step** focuses on the identification of potential wind turbine areas within satellite imagery. We applied a threshold of 0 to delineate the target wind turbine area and obtained binary images of potential wind turbines. In the **fourth step**, we performed preliminary processing of wind turbine images through morphological erosion and expansion. The **fifth step** consists of two post-processing stages. First, spatial filtering was executed based on the spatial clustering distribution characteristics of offshore wind turbines to eliminate noise[17,18]. Second, we filtered out implausible wind turbine points by considering the time-series consistency of the wind turbines. The **final step** involves the classification of wind farms. A wind farm typically comprises multiple wind turbines that are spatially clustered together[19,20]. We employed the density-based spatial clustering method DBSCAN[21] to group neighboring wind turbines into the same wind farm.

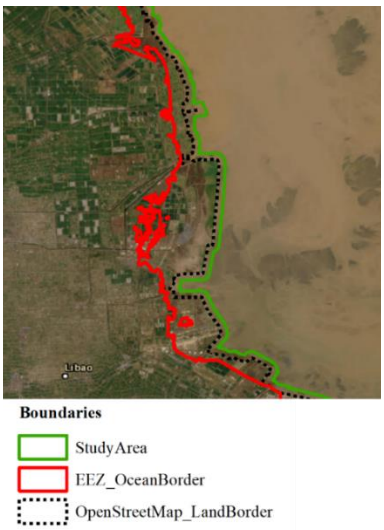

Fig. S1.3 Improvement of study area boundary

1) Step 1 Modification of study area boundary

The methodology for extracting wind turbines, as outlined in the literature[16], has a strong dependence on the offshore boundary. It's particularly sensitive to structures that resemble wind turbines, such as buildings and bridges. To mitigate the impact of land-adjacent features, we implemented a modification to the study area boundary. Instead of relying solely on the EEZ to define the offshore area of the Chinese mainland, we took a more precise approach (Fig. S1.3). To further minimize terrestrial influences, we established a 1-kilometer buffer zone along the land boundary of OSM and intersected it with the EEZ. This intersection defined the final study area for our research. This approach ensures a more accurate representation of the offshore area, addressing the challenges posed by the junction of land and sea in the dataset.

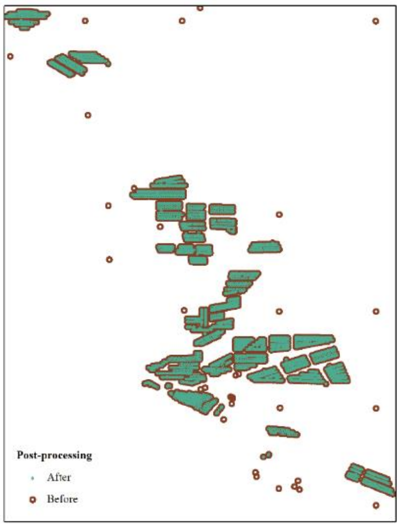

Fig. S1.4 Results of before and after Post-processing

2) Step 2 Percentile-based yearly composite image

To address the challenge of differentiating between offshore wind turbines and floating or temporarily moving objects, such as ships and boats, within the Sentinel 1 imagery, we employed a percentile-based approach. Using statistical tools available in Google Earth Engine [16,22], we created annual synthetic imagery by calculating the percentile and interval mean between 80-100% when using the 'intervalMean()' reduction function. This synthetic imagery was instrumental in distinguishing these objects based on their frequency of appearance in the time-series imagery. By analyzing annual Sentinel-1 time series images spanning from 2015 to 2022, we could effectively identify and isolate the stable features, namely offshore wind turbines, from the dynamic and transient objects.

3) Step 3 Image thresholding

To effectively identify offshore wind turbines in SAR images, it's crucial to consider their high backscatter characteristics. In Sentinel-1 data, wind turbines exhibit image values greater than 0[23]. To narrow down the target area of wind turbines, we applied a threshold of 0. This threshold was instrumental in isolating the wind turbine features within the imagery (Formula S1).

$$Composite\ Image = \begin{cases} 0 & Pixel\ Value \leq 0 \\ 1 & Otherwise \end{cases} \qquad Formula\ S1$$

4) Step 4 Morphological erosion and dilation

After applying the threshold to suppress undesired features, some stable targets persisted in the remaining region of the binary images. To enhance the high backscatter image objects corresponding to wind turbines, we conducted morphological erosion and expansion operations. Following this, we implemented an area size range filtering algorithm to further refine the results. This algorithm ensured that objects falling outside the size range of 20 to 200 pixels were eliminated, effectively removing oversized and undersized objects, such as islands, oil platforms, and small noisy artifacts, in alignment with the approach outlined in the literature[16].

5) Step 5 Post-processing

Following the initial wind turbine identification and area size range filtering, we conducted two additional post-processing steps to refine and filter the final wind turbine dataset.

a. Spatial filtering with a 3km buffer zone

We conducted spatial filtering to leverage the spatial clustering distribution characteristics of offshore wind turbines, as suggested by previous research[17,18], as illustrated in Fig. S1.4. We applied a 3 km buffer zone to the dataset to eliminate scattered points that were not indicative of wind turbine sites. Specifically, each identified point was considered a wind turbine site only if it had at least three neighboring points within the 3 km buffer.

b. Time serials filtering with wind turbine consistency

Considering that China's first offshore wind farm was established in 2008[24], we assumed that wind turbines were not decommissioned. Thus, we expected that wind turbines built in a particular year would continue to appear in subsequent years[25]. To implement this assumption, we introduced the following method: assuming WT_t represents a wind turbine at time t, and

WT_{t+1} represents the wind turbine at the next interval, time t+1. We intersect the wind turbine point WT_{t+1} with WT_t, if WT_t does not appear in the proximity of the position of WT_{t+1}(as defined by Formula S2), it is not considered an additional wind turbine and is subsequently removed from the dataset.

$$WT_t = \begin{cases} include, Intersect(WT_{t+1}, WT_t) == yes \\ exclude\,, \qquad\qquad\qquad\qquad Otherwise \end{cases} \qquad Formula\ S2$$

6) Step 6 DBSCAN clustering

Among the various spatial clustering algorithms available, Density-Based Spatial Clustering of Applications with Noise (DBSCAN)[26] is renowned for its capability to identify clusters of arbitrary shapes while effectively handling noise. In our study, we harnessed the Density-Based Clustering (DBSCAN) tool within ArcGIS Pro 3.1.0 to cluster wind turbines based on their spatial density (Fig. S1.5). Each unique cluster is denoted by a different color, representing distinct wind farms within the dataset.

Fig. S1.5 DBSCAN clustering

7) Step 7 Validation of wind turbines extraction

The validation data, detailed in the annex, were meticulously obtained through manual visual interpretation based on a combination of multi-source data. These sources included Sentinel-1 satellite imagery, the highest-quality imagery accessible through Google Earth Pro, and the 4C offshore dataset. The resulting validation dataset, depicted in Fig. S1.6 with Sentinel image and Google Earth image, encompasses a total of 18 wind farms and 1365 turbines. Of these, seven wind farms were updated in 2021 from the Global Offshore Wind Turbine Validation Datasets of mainland China[16], with the number of wind turbines expanding to 421 in 2022. Additionally, we incorporated an additional 11 wind farms and 944 wind turbines into the dataset. These selected wind farms were deliberately distributed across the offshore area of mainland China to ensure the comprehensiveness and validity of the validation data. The extraction accuracies of the two validation datasets are presented in Table S1.1, with an overall accuracy rate averaging an impressive 97.11%.

Table S1.1 Precision of wind turbine extraction

	Total	Correct of WT	Error of WT	Precision
GOWT Validate Data	421	410	11	97.38%
Additional Validate Data	944	914	30	96.82%

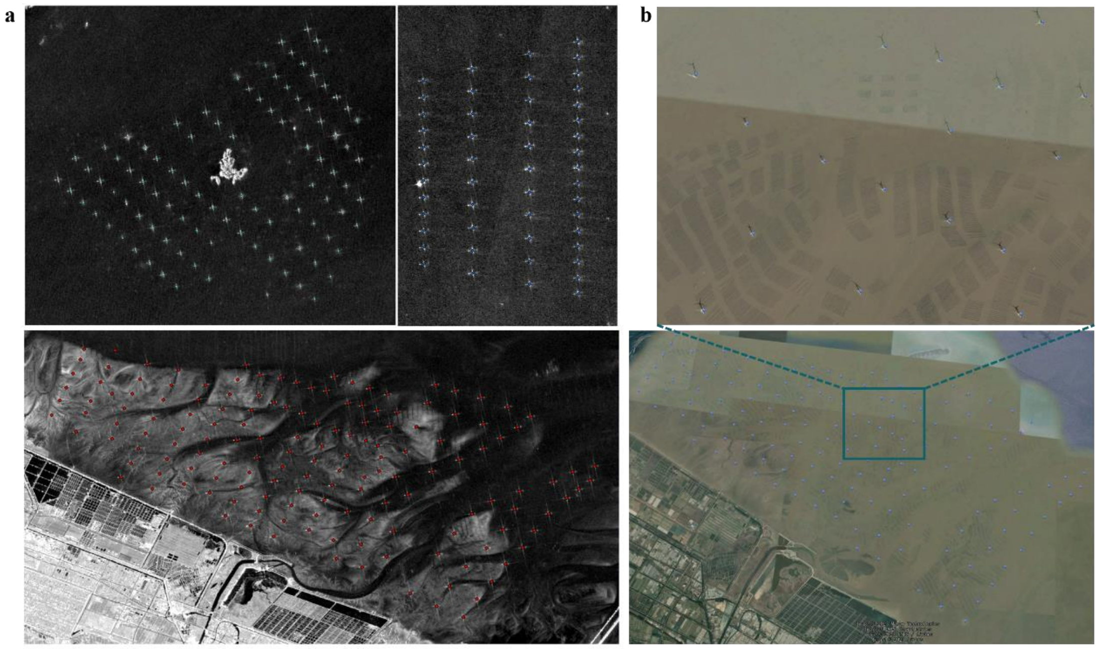

Fig. S1.6 Validation data (a) Sentinel-1 image. (b) Google Earth image.

S1.3.2 Offshore distance

To determine the offshore distance of each wind turbine, we utilized the wind turbine point data in conjunction with the land boundary. Specifically, we calculated the closest geographic distance from each wind turbine to the land boundary, thereby establishing the offshore distance for each wind turbine. This calculation was performed using ArcGIS Pro 3.1.0, as depicted in Fig. S1.7.

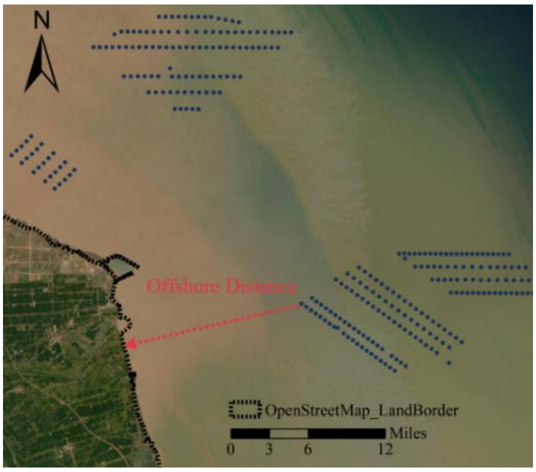

Fig. S1.7 Offshore distance

S1.3.3 Installation date

The installation date of each wind turbine during 2015 and 2022 are shown in Fig. S1.8. It is essential to note that we categorized the installation dates of wind turbines built in 2015 and earlier as "~2015".

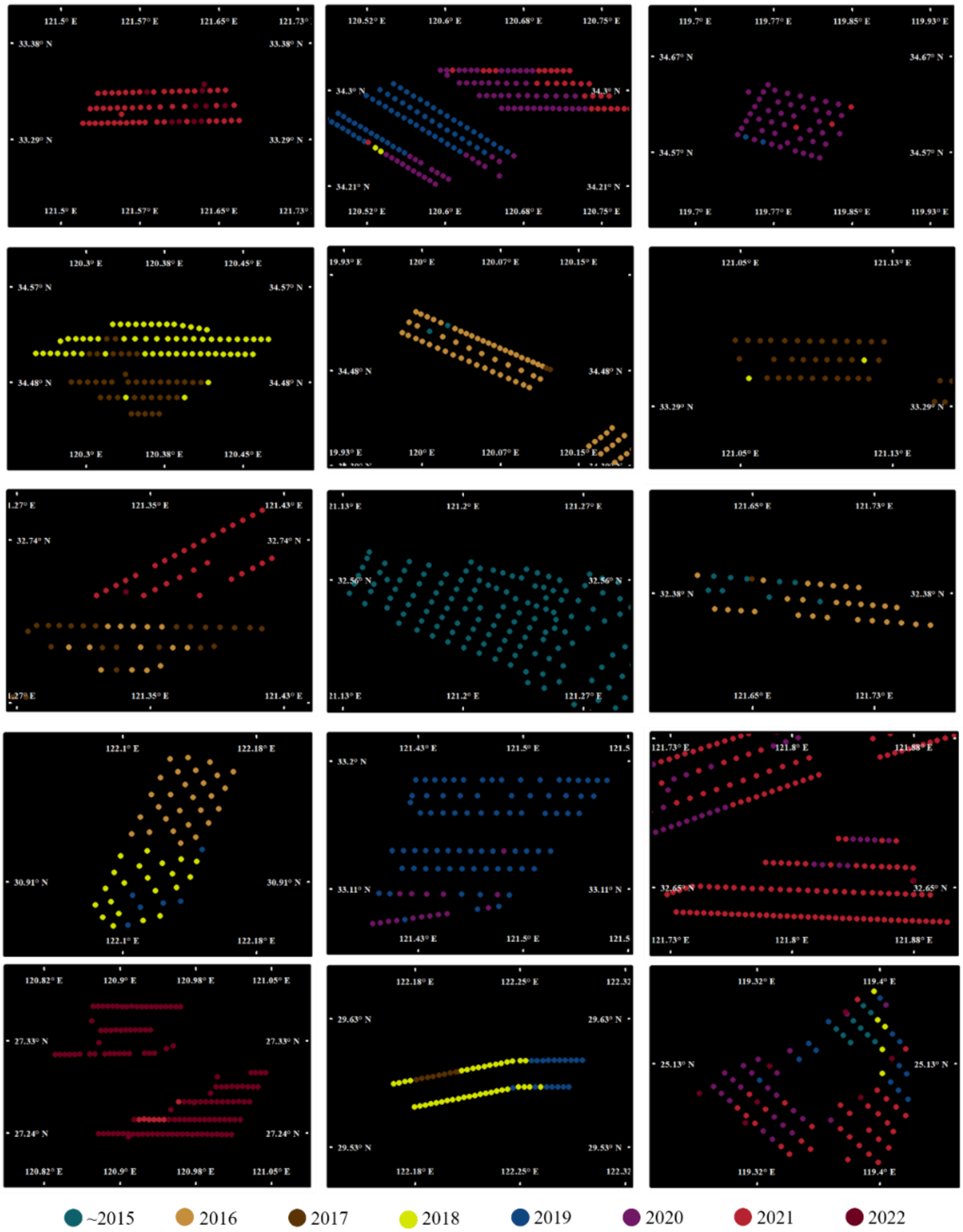

Fig. S1.8 Installation date

S1.4 Measurement data of wind turbine acquisition

S1.4.1 Height

The location of both the layover effect points and the wind turbines serves as critical parameters in the calculation of wind turbine height, as illustrated in Fig. S1.9. While we've already extracted the wind turbine locations as described in S1.3.1, the crucial step in the height calculation process involves obtaining the layover effect points required for the $Dist$ calculation.

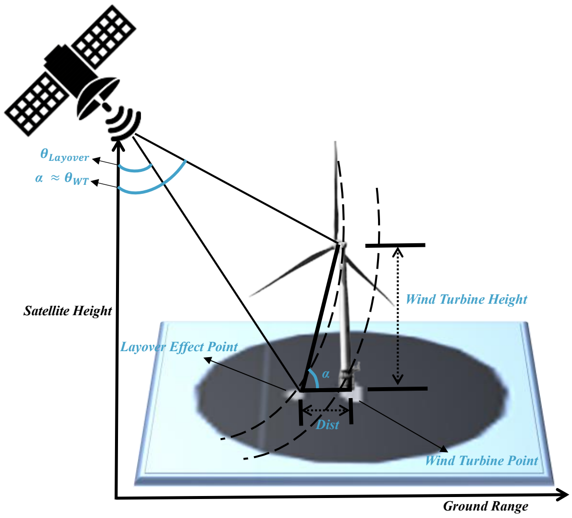

Fig. S1.9 Height calculation from Sentinel-1 images

The process for determining the height of wind turbines is outlined in Fig. S1.10 and entails the following steps:

Defining the target image area: To reduce computational effort, we initially established a 300-meter buffer zone around each offshore wind turbine. This buffer zone served as the target image area for height calculation.

Automated thresholding: Given that the distribution of image values within the wind turbine region falls within the range of [-15,15] (as depicted in Fig. S1.11), we automated the thresholding process. A range of thresholds was generated by incrementally adding a span value (set to 5) within the range of -15 to 15. For each threshold, a binary image was computed.

Optimal threshold selection: To identify the optimal threshold, we calculated the minimum residual sum of squares using Formula (1) between the computed heights and observed data[12]. This process involved iterating through the thresholds. The threshold that exhibited the highest frequency and minimized the sum of squares of the residuals was selected as the best threshold, which was subsequently used to generate the final binary image.

Identification of layover effect points: Since the pixel area of the layover effect points is significantly smaller than that of the wind turbines in the binary image, we identified connected areas with fewer than 20 pixels as layover effect points, which is essential for calculating the distance to wind turbines.

Calculation of geographical distance ($Dist$): Using the identified layover effect points and wind turbine locations, we determined the geographical distance ($Dist$) between these points.

Deriving α: The value of α was obtained from the original bands of Sentinel-1 images available through Google Earth Engine.

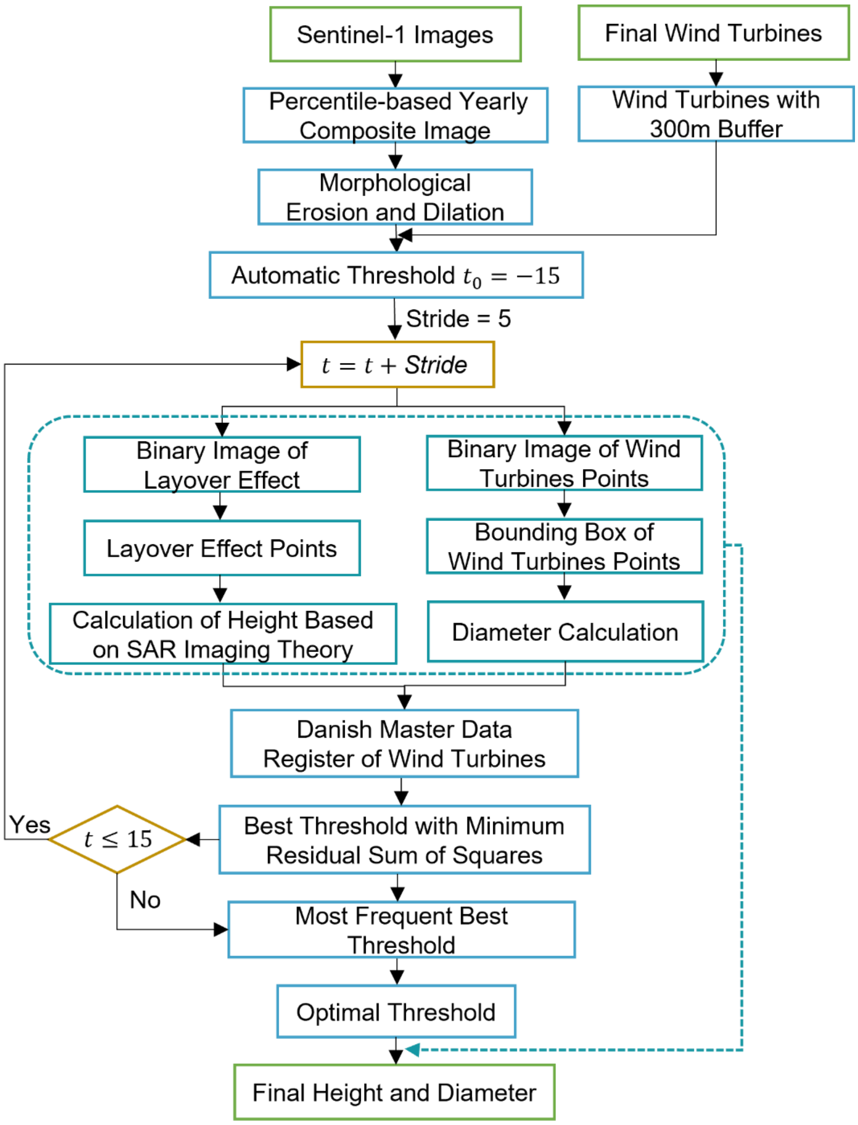

Fig. S1.10 Flowchart of automatic threshold fitting for height and diameter

Height calculation: With all the necessary parameters in place, the height of wind turbines was calculated using a specified formula.

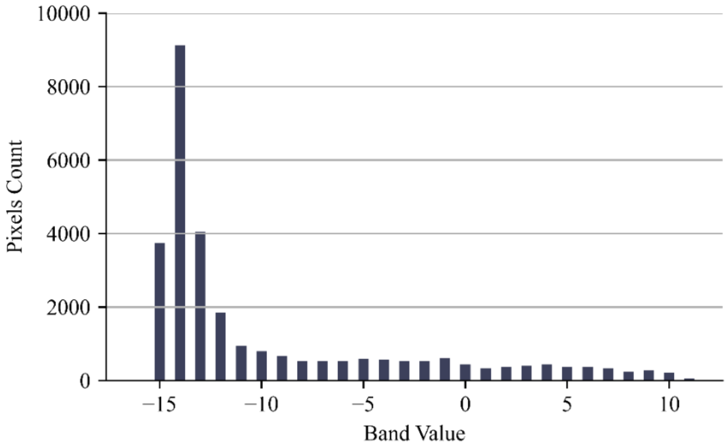

Fig. S1.11 Distribution of Sentinel-1 image value

The minimum residual sum of squares and definition of optimal threshold are calculated as Formula S3:

$$J(T) = Min\left(\left(\sum_{i=0}^{m}\left(Height_{Cali} - Height_{Openi}\right)^2\right)_t\right) \quad Formula\ S3$$

This function, denoted as $J(T)$, is employed to obtain the optimal threshold T, m representing the number of wind turbine points within the wind farms, t signifies the automatic threshold of the image, falls within the range $t\epsilon[-15,15]$. When the automatic threshold value is t, $Height_{Cali}$ and $Height_{Openi}$ are the height of wind turbines calculated via formula and the height data in public dataset respectively for the i-th wind turbine point.

Table S1.2 Optimal threshold frequency of height and diameter

	-15	**-10**	**-5**	**0**	**5**	**10**	**15**
Height	7	5	0	0	2	0	0
Diameter	0	1	0	12	1	0	0

The determination of the optimal thresholds for both height and diameter followed a similar methodology. These optimal thresholds were essential for accurate calculations. The results for the height and diameter of mainland China were rigorously evaluated using data from The Wind Power and 4C Offshore. Table S1.2 presents the statistical details of the optimal thresholds for height and diameter across the 14 wind farms[12]. In this analysis, the optimal image threshold for calculating height was found to be -15, while the threshold for calculating diameter was set at 0. These determined thresholds were subsequently utilized in the calculation of the height and diameter of offshore wind turbines in mainland China, ensuring the accuracy of the results.

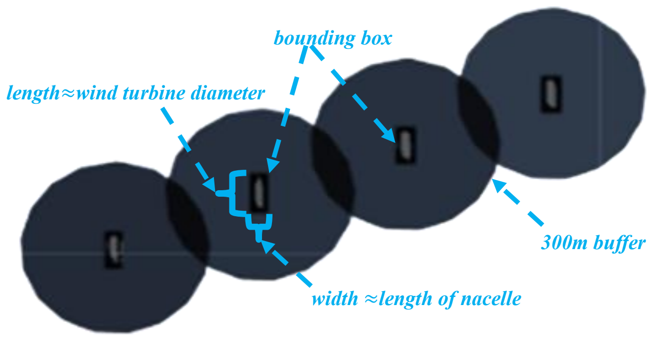

Fig. S1.12 Bounding box of wind turbines

S1.4.2 Diameter

Formula S4-S5 illustrate the connection between the length of the bounding box and the rotor diameter, as well as the width and the nacelle length. These formulas are integral to the calculation of wind turbine properties. To facilitate this calculation, we directly obtain the Area a and perimeter p of the bounding box using tools available on Google Earth Engine. This information plays a crucial role in accurately determining the dimensions of the rotor diameter and nacelle length for each wind turbine.

$$Length = Max\left(\frac{p}{2} - \sqrt{\frac{p^2}{4} - a}\,, \sqrt{\frac{p^2}{4} - a}\right) \quad Formula\ S4$$

$$Width = Min\left(\frac{p}{2} - \sqrt{\frac{p^2}{4} - a}\,, \sqrt{\frac{p^2}{4} - a}\right) \quad Formula\ S5$$

Where $Length$,$Width$,a,p are the length, width, area and perimeter of the bounding box respectively.

To assess the accuracy of our predicted wind turbine heights and diameters for mainland China, we conducted a thorough comparison with data from 2629 wind turbine points sourced from The Wind Power and 4C Offshore. The evaluation was based on key statistical metrics, including the R-value and RMSE. The specific results and values of these metrics are presented in Fig. S1.13a and Fig. S1.13b, providing insights into the performance of our predictions.

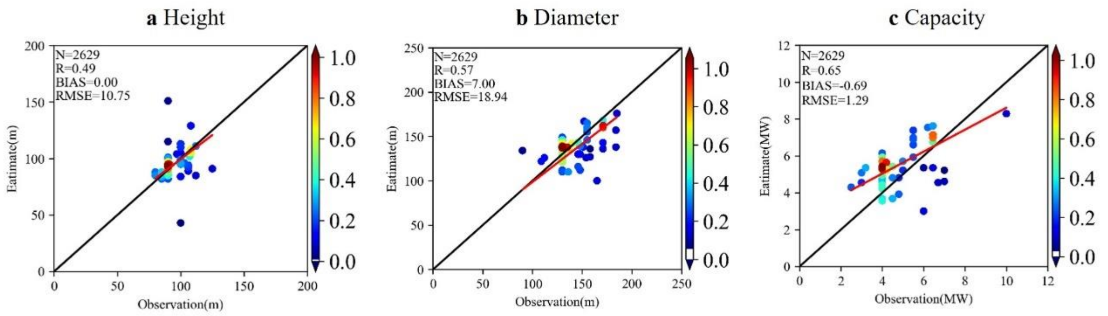

Fig. S1.13 R-value and RMSE of (a) height (b) diameter (c) capacity

The R-values obtained for height and diameter in our evaluation are 0.49 and 0.57 respectively, with corresponding root mean square errors (RMSE) of 10.75 meters and 18.94 meters. Notably, considering the resolution of Sentinel-1 data at 10 meters per pixel, our analysis demonstrates an average identification error for height and diameter that is well-controlled within two pixels. This level of accuracy underscores the robustness and reliability of our approach in calculating wind turbine heights and diameters, further affirming the precision of our results.

S1.4.3 Capacity

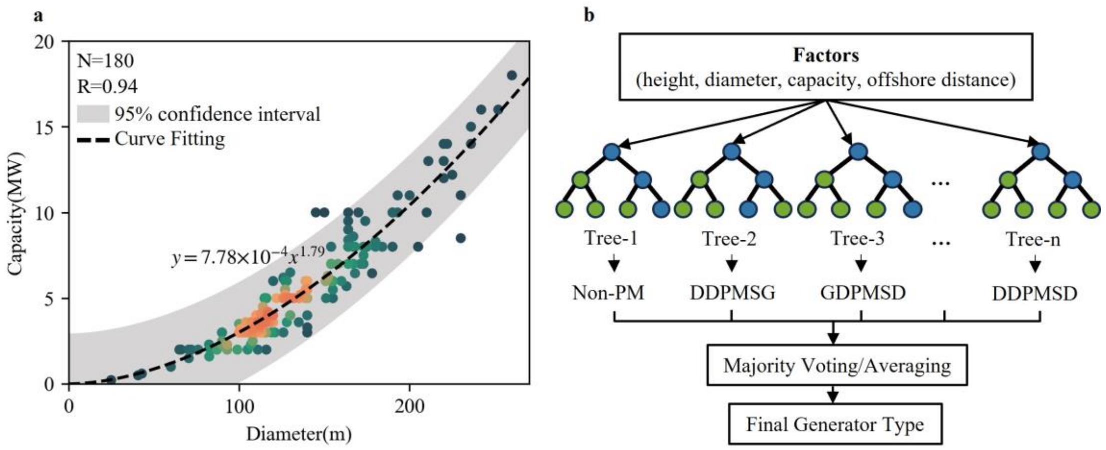

Fig. S1.14 Regression model and Random Forest classifier (a) Regression model between diameter and capacity, where x and y represent diameter and capacity, N and R denote the number of data points and correlation coefficient. (b) Random Forest classifier for generator types.

S1.5 Component and material stocks quantification

S1.5.1 Generator type classification

Based on wind turbine models and manufacturers from The Wind Power, we conducted a comprehensive search across various online dataset sources, particularly Wind-turbine-models and public reports, to gather generator type information for each wind turbine. After filtering out data lacking generator type details, our final dataset comprises 253 wind turbines, each defined by four crucial factors: diameter, capacity, height, and offshore distance. We then compiled this dataset to build a Random Forest classifier.

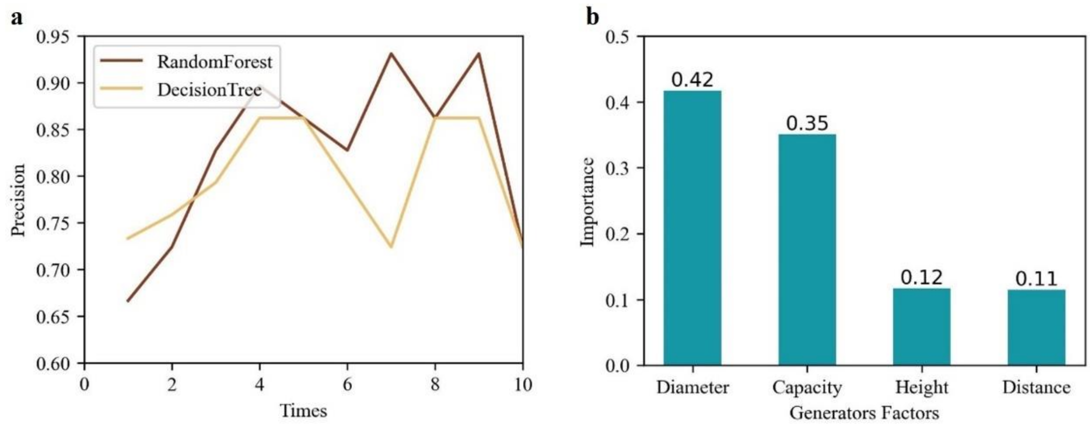

Fig. S1.15 Generator type classification (a) Ten-fold cross-validation results of decision tree and Random Forest. (b) Ranking of importance of generator type factors.

The dataset was split into a training set and a testing set, with a ratio of 7:3, comprising 177 and 76 wind turbines, respectively. We employed ten-fold cross-validation to evaluate the performance of two common machine learning classifiers, Decision Tree and Random Forest. The results, as depicted in Fig. S1.15a, demonstrated that the Random Forest classifier outperformed the Decision Tree on the dataset, achieving a final classification accuracy of 86.36%. Subsequently, we utilized the Random Forest classifier to identify the generator types of wind turbines in the offshore areas of mainland China. Additionally, we analyzed the importance of the four key factors (diameter, capacity, height, and offshore distance) concerning generator types. As illustrated in Fig. S1.15b, the analysis revealed that diameter and capacity exerted the most significant influence on generator type, followed by height and offshore distance.

The results of the generator type classification in mainland China are visualized in Fig. S1.16. In the figure, 'predicted generator types' represent the generator type of wind turbines predicted by our classifier, while 'observed generator types' denote the data sourced from The Wind Power.

Overall, the classification process yielded accurate results for the majority of turbine types. However, there were some instances of misclassification, particularly between non-PM and DDPMSG, as well as between DDPMSG and GDPMSG. This misclassification can be attributed to the similarities in diameter, capacity, height, and offshore distance between non-PM and DDPMSG, as well as between DDPMSG and GDPMSG, which poses a challenge in clearly distinguishing between these closely related categories.

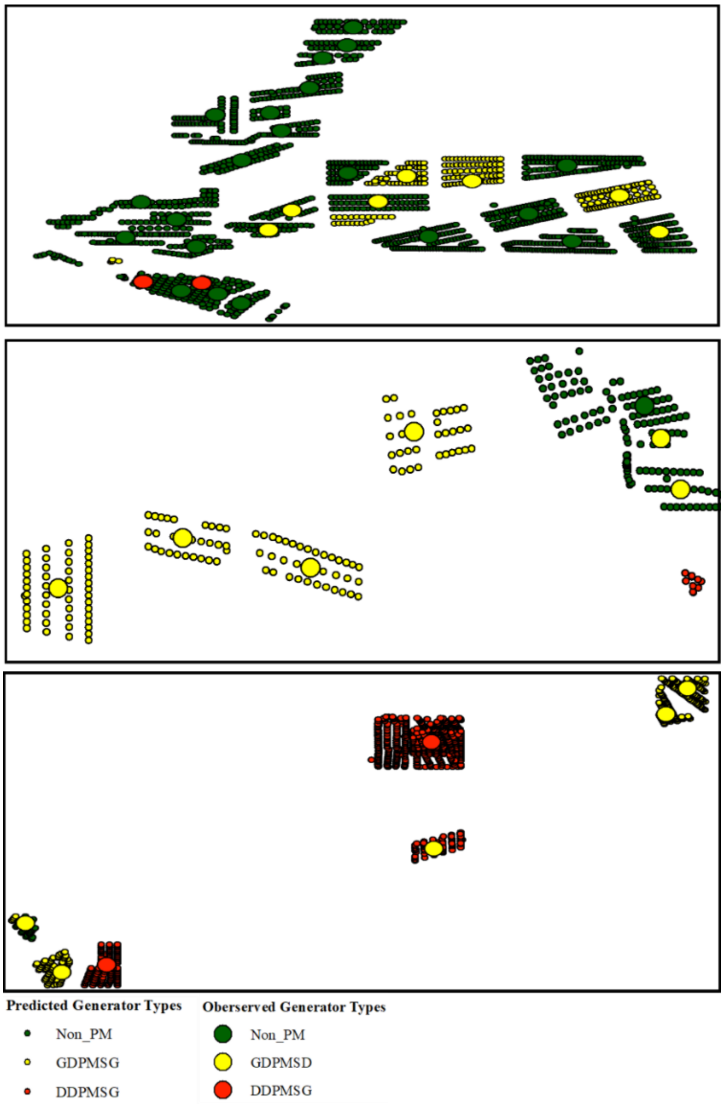

Fig. S1.16 Generator type classification

S1.5.2 Material percentages and intensities

Submarine cables used in wind farms encompass both export cables and inter-array cables[27]. Inter-array cables play the role of collecting power generated by wind turbines and transmitting it to collector platforms within the wind farm. Export cables are responsible for transmitting power from the wind farm's power plants to the existing main grid at the onshore interconnection point. To estimate the distance of export cables, we estimated the stock of export submarine cables based on an approximation of the offshore distance, by calculating the average offshore distance of all turbines within the same wind farm. The stock of export cables was then determined using Formula S6.

$$Stock_{Export} = OffshoreDistance_{mean} * MI_{Export} \quad Formula\ S6$$

the Where, $Stock_{Export}$ represents in-use stock of export cables, $OffshoreDistance_{mean}$ represents average value of offshore distance in the wind farm. MI_{Export} represents export cables material intensity.

In our approach to calculating the total length of inter-array cables, we employed a compromise method. Considering that the average distance between offshore wind turbines is approximately 1.5 kilometers[28], we assumed a series connection between each turbine. As a result, the number of cables required between turbines is equal to the total number of turbines minus 1. This allowed us to derive the final stock of inter-array cables using Formula S7.

$$Stock_{Array} = (Number(WTs)) * 1.5km * MI_{Array} \quad Formula\ S7$$

Where, $Stock_{Array}$ represents in-use stock of inter-array cables, $Number(WTs)$ indicates the number of wind turbines in the wind farm, and $1.5km$ is the approximate distance between offshore wind turbines. MI_{Array} represents export cables material intensity.

Table S1.3 Material intensity (t/km) of submarine power cables

	Aluminum	Copper	Steel	Total Weight
Array	8.2	0.7	11.2	32.3
Export	15.5	1.2	16.8	62.2

Table S1.4 Percentages of bulk materials in components (%)

	Rotor	Nacelle			Tower
		Non-PM	DDPMSG	GDPMSG	
Low alloyed steel	9. 8	16.6	8.9	10.3	97.1
High alloyed steel	9.4	38.6	29.8	39.3	-
Cast iron	25.8	35.6	52.6	41.5	-
Aluminum	0.1	1.05	0.9	0.9	1
Copper	0.1	2.65	2.2	2.2	0.9
Electrics/Electronics	-	0.45	0.1	0.4	1
Other materials	54.8	5.05	5.5	5.4	0

Taking into account the material intensity with minimal change over time due to turbine technology development[29], and the recent surge in Chinese offshore wind turbines[30], we used the material intensity of rare earth material intensity in 2020 to calculate the three rare earth elements stocks, factoring in capacity, generator type, and material intensity.

Table S1.5 Baseline rare earth material intensity in 2020 ($kg \cdot MW^{-1}$)

	Nd	Dy	Pr
DDPMSG	175.5	29.3	43.9
GDPMSG	32.4	5.4	8.1

S1.6 Results validation

We collected data on the number, capacity, and stock of offshore wind turbines in mainland China from various reports and references. It's important to note that our validation process was influenced by the constraints of a lack of publicly available data and the low comparability between various components and materials. Consequently, we could only identify a single representative for each category, specifically, cables and steel, for our comparison. In our analysis, we used stock information for submarine cables and steel as a proxy for components and materials. These choices were made due to their widespread relevance and greater availability (Table S1.6).

Table S1.6 Comparison of magnitude in number, capacity and stocks

	Number of WTs	Accumulated Capacity (GW)	Stock of Submarine Cables(kt)	Stock of Steel (*10kt)
This Study	5921	33	154.38	340(Foundations Excluded)
Other Sources	5700[30]	31.44[31]	130.68[32]	627[33]

S2 Results

S2.1 Submarine cable stocks

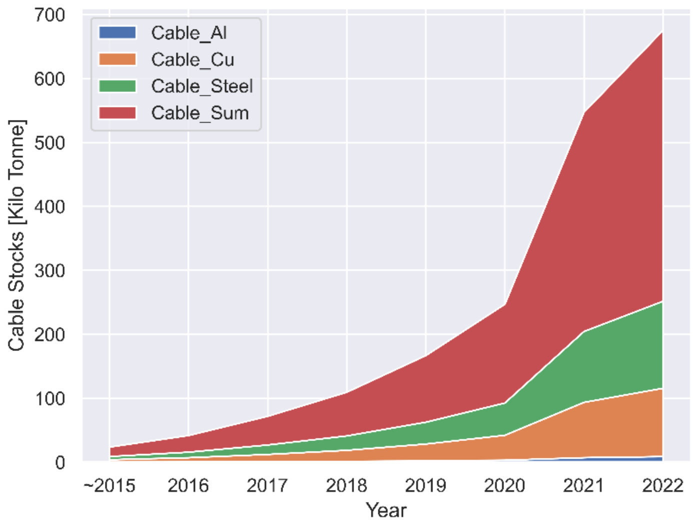

Fig. S2.1 Submarine cable stocks during 2015-2022

S2.2 Primary components in-use stock of wind turbines

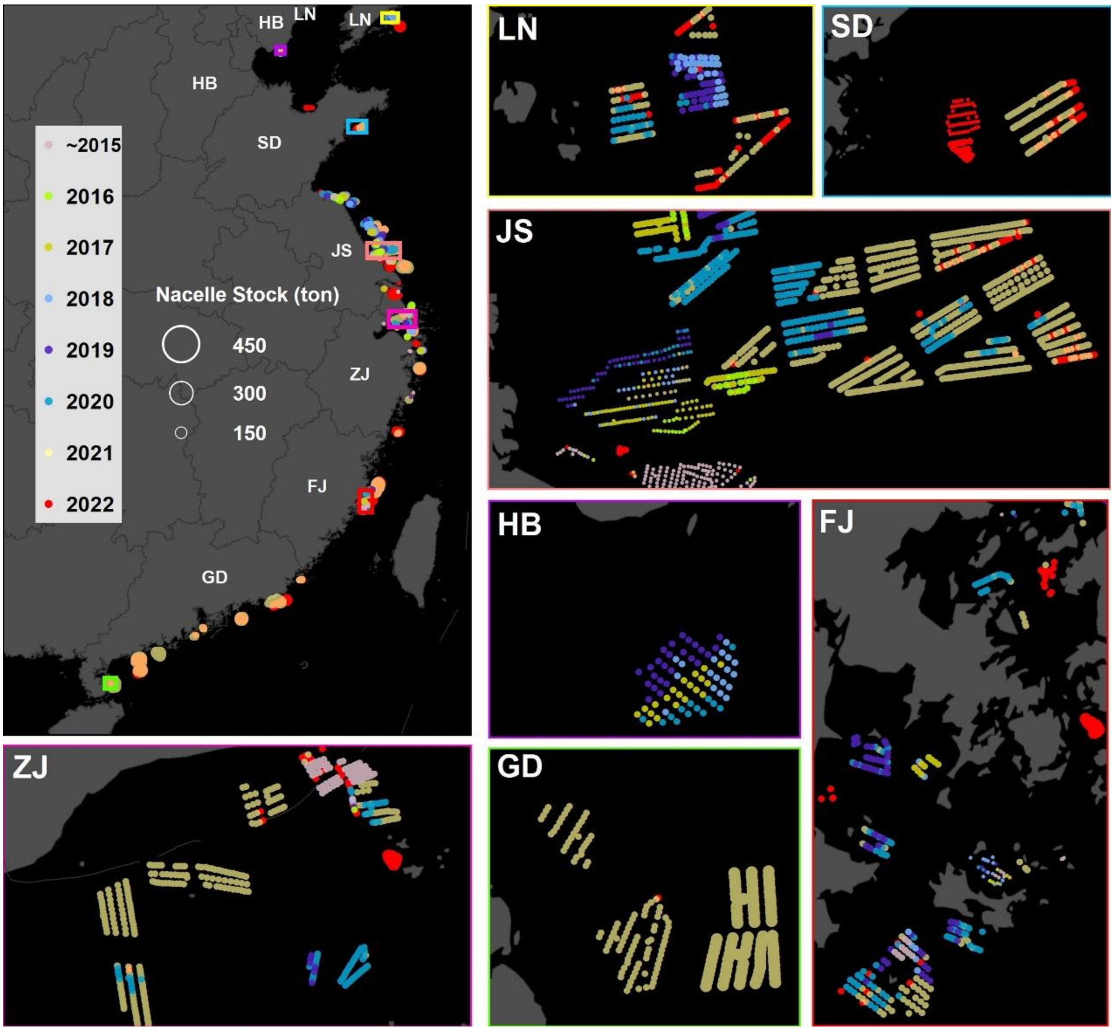

Fig. S2.2 Stock map of nacelle

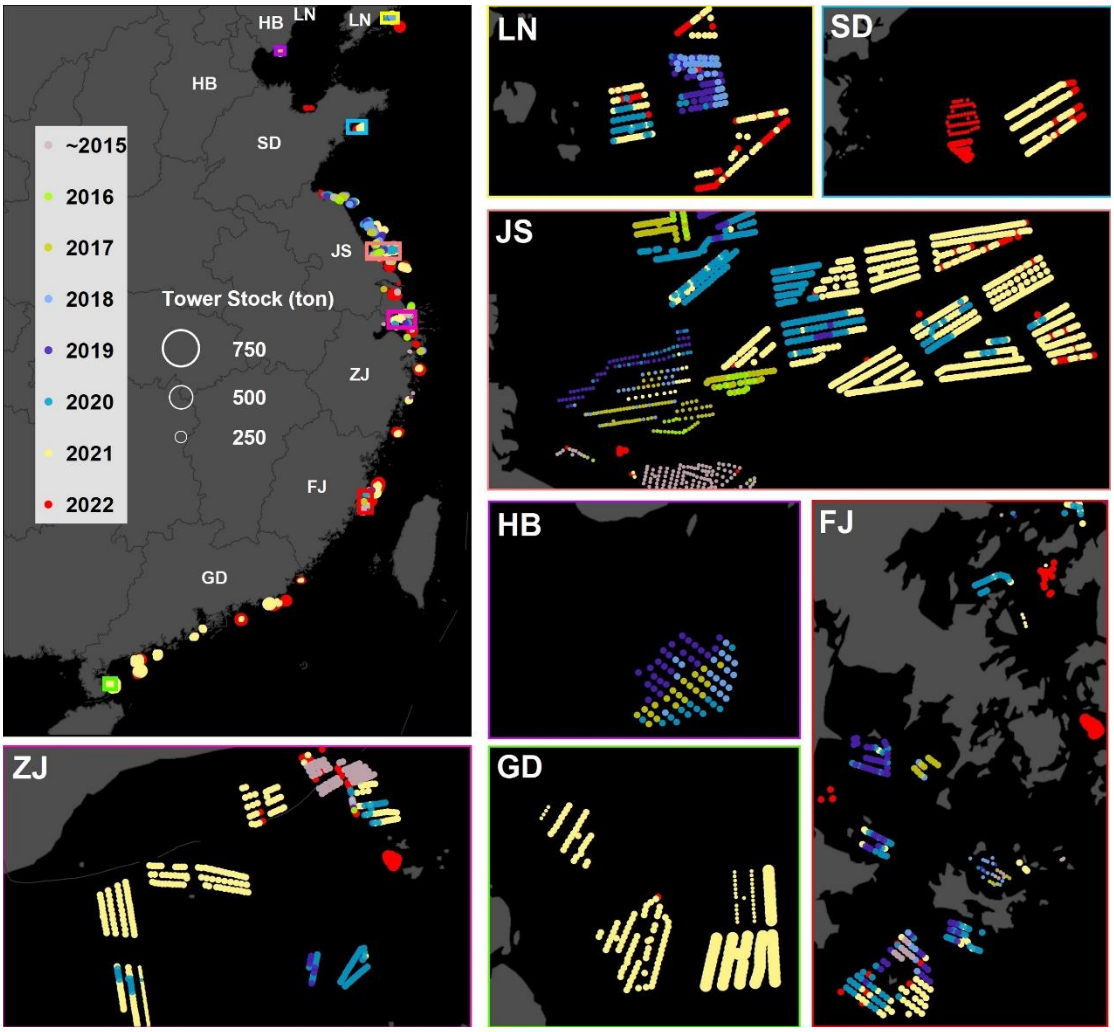

Fig. S2.3 Stock map of tower

S2.3 Critical material in-use stock of wind turbines

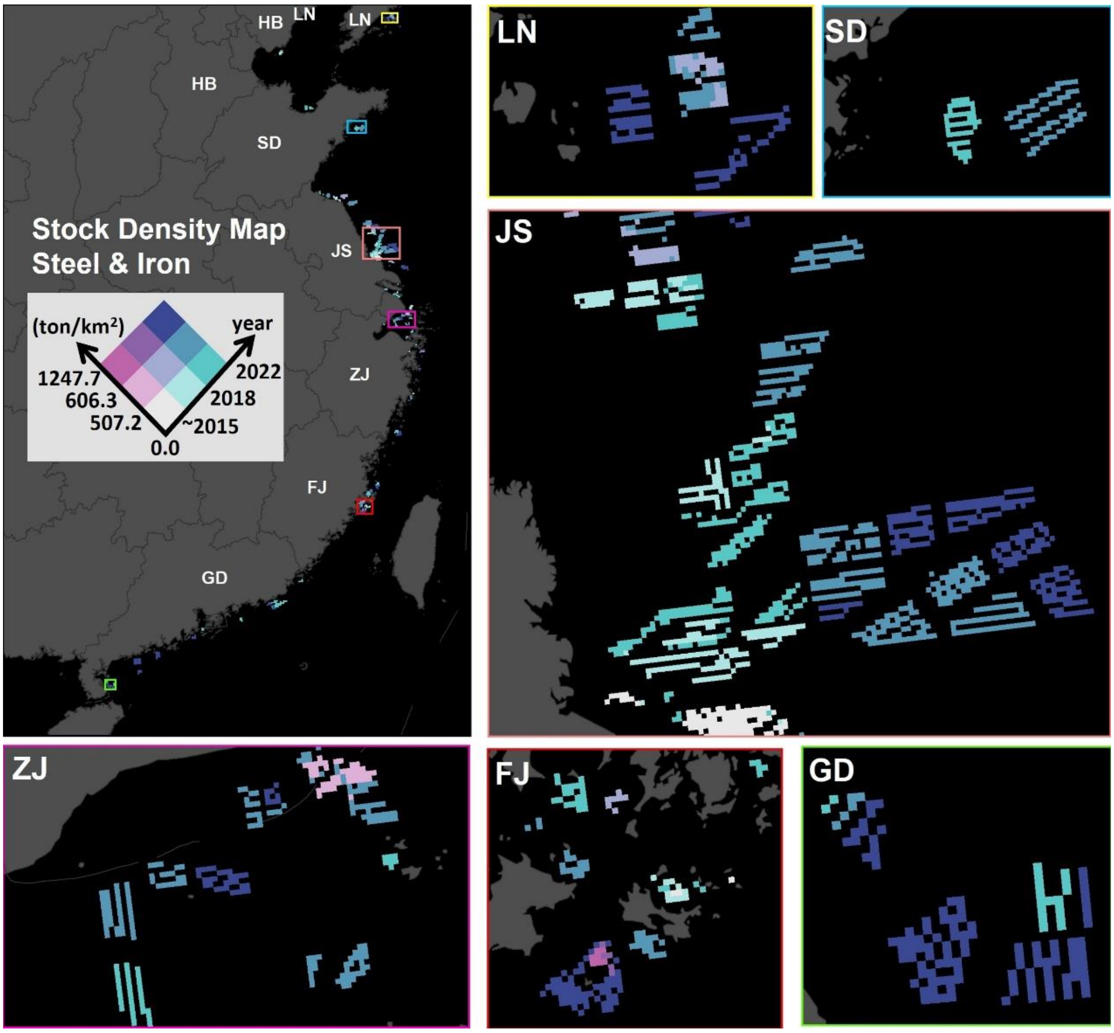

Fig. S2.4 Stock density map of steel & iron

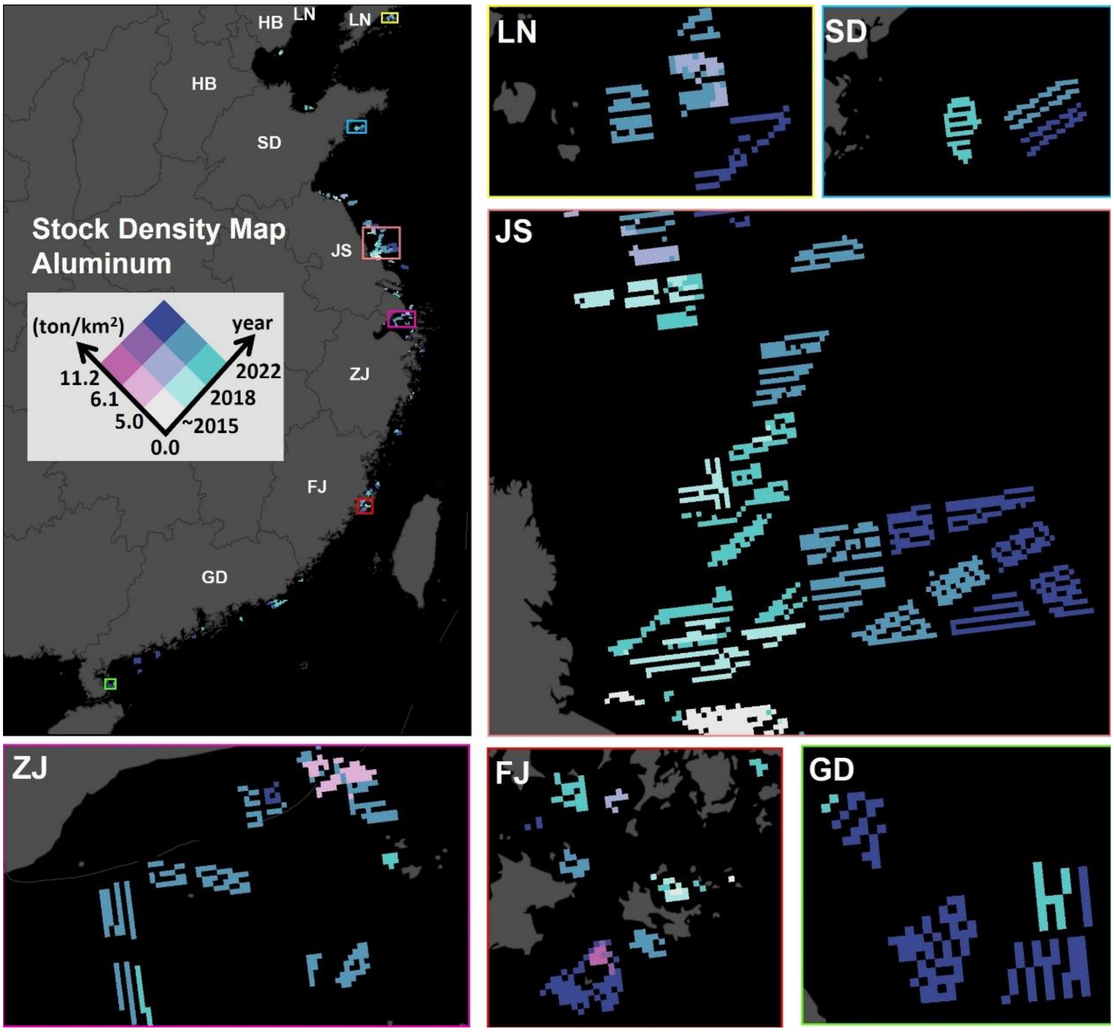

Fig. S2.5 Stock density map of aluminum

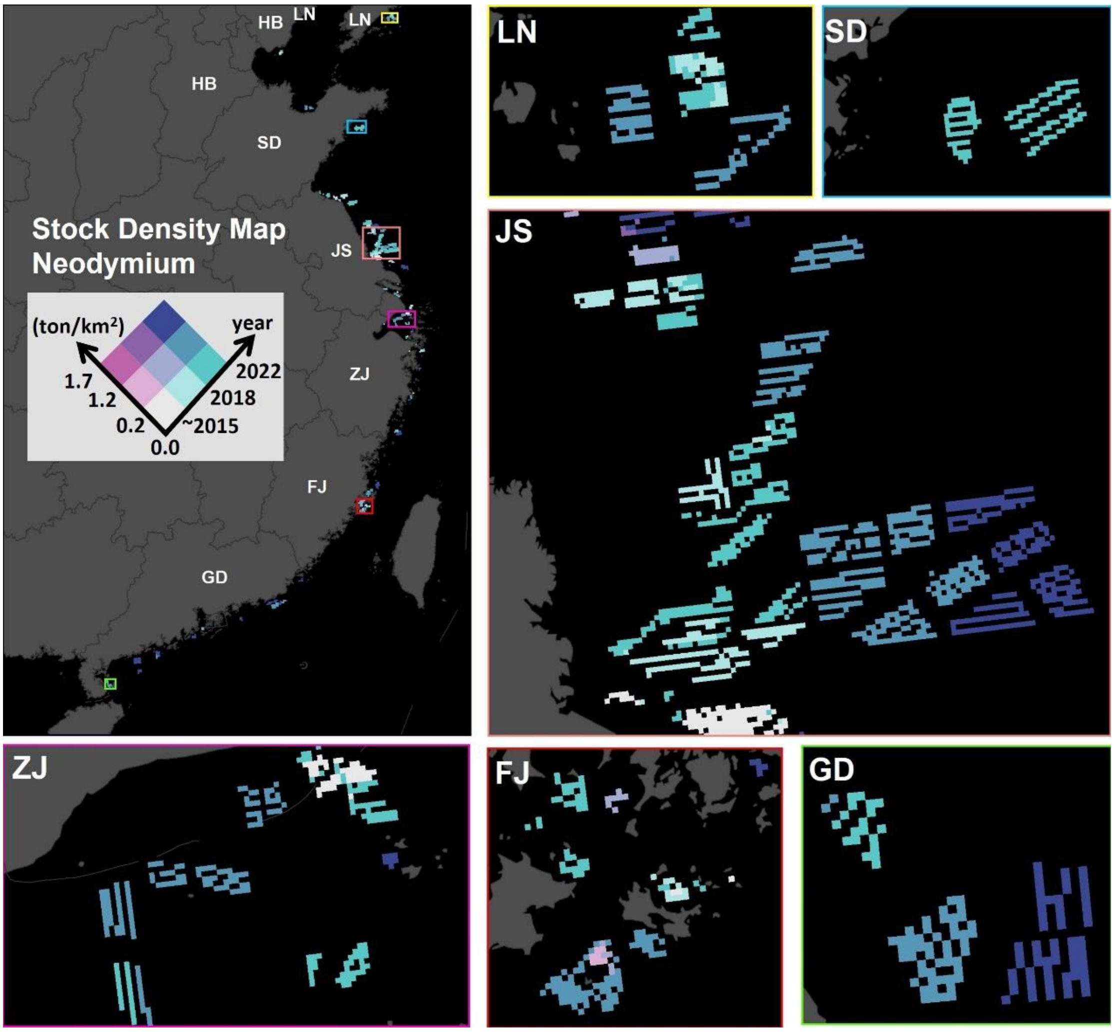

Fig. S2.6 Stock density map of Neodymium

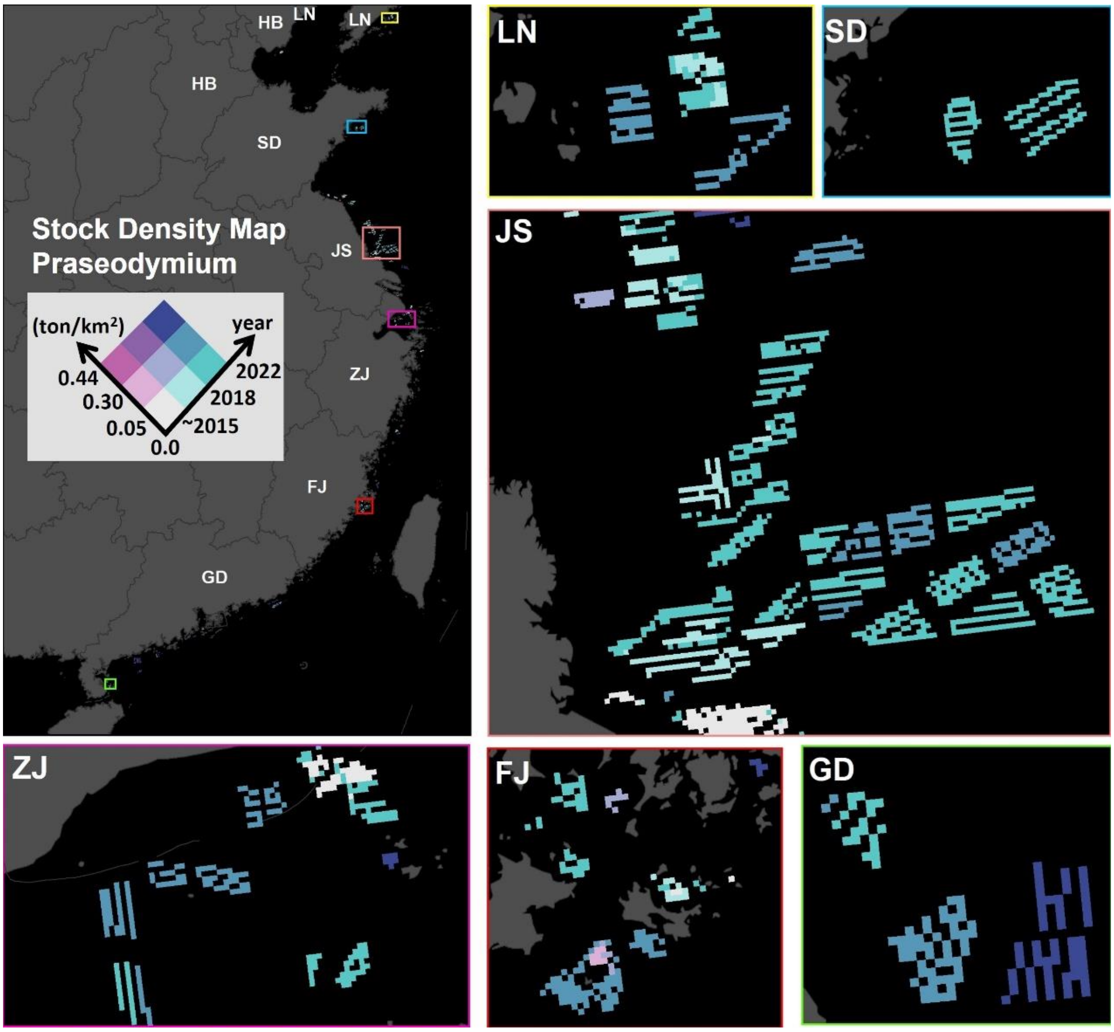

Fig. S2.7 Stock density map of Praseodymium

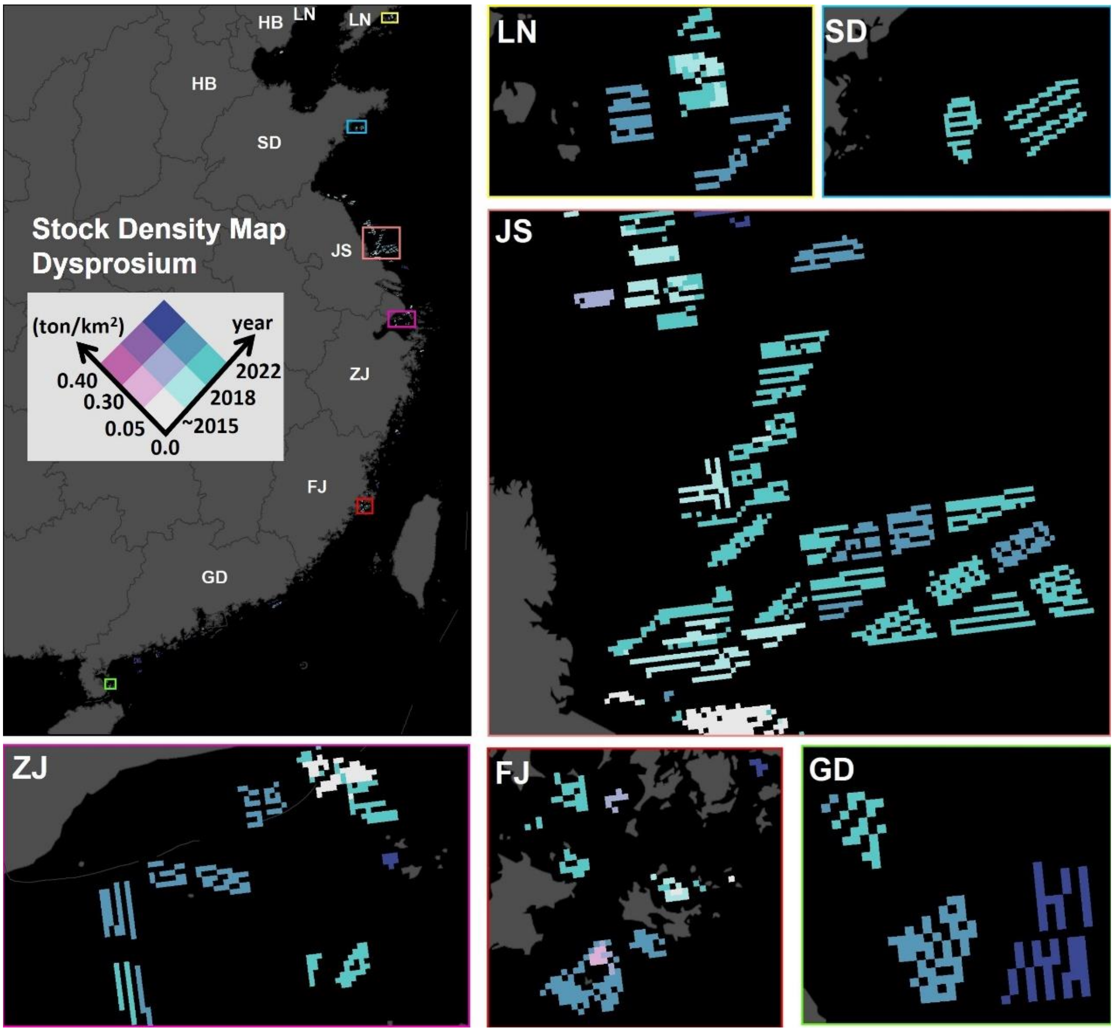

Fig. S2.8 Stock density map of Dysprosium

S2.4 Offshore wind turbine in-use stock dataset

Table S2.1 Offshore wind turbine in-use stock dataset

Items	Contents
Geographic Scope	Mainland China
Time Range	2015-2022
Number of Wind Turbines	5921
Attributes	① Location ② Commissioning Date ③ Tower Height ④ Rotor Diameter ⑤ Offshore Distance ⑥ Capacity ⑦ Generator Type

Stocks	Components Stocks ① Rotor Stock ② Nacelle Stock ③ Tower Stock ④ Submarine Cables Stock Material Stocks ① Bulk Material Stocks (low alloyed steel, high alloyed steel, cast iron, copper, aluminum, electrics/electronics, other materials) ② Rare Earth Material Stocks Neodymium, Dysprosium and Praseodymium
Data Format	Shapefile (Point)

Supplementary References

1. Liang, Y. et al. Estimation of the influences of spatiotemporal variations in air density on wind energy assessment in China based on deep neural network. *Energy*. **239**, 122210 (2022).
2. Cao, Z. et al. Resourcing the fairytale country with wind power: a dynamic material flow analysis. *Environ. Sci. Technol.* **53**, 11313-11322 (2019).
3. Chen, Z., Kleijn, R. & Lin, H. X. Metal Requirements for Building Electrical Grid Systems of Global Wind Power and Utility-Scale Solar Photovoltaic until 2050. *Environ. Sci. Technol.* **57**, 1080-1091 (2023).
4. Rinaldi, K. Z., Dowling, J. A., Ruggles, T. H., Caldeira, K. & Lewis, N. S. Wind and solar resource droughts in California highlight the benefits of long-term storage and integration with the western interconnect. *Environ. Sci. Technol.* **55**, 6214-6226 (2021).
5. Verma, S., Paul, A. R. & Haque, N. Assessment of materials and rare earth metals demand for sustainable wind energy growth in India. *Minerals*. **12**, 647 (2022).
6. You, R., Yuan, X. & Li, X. A multi-rotor medium-voltage wind turbine system and its control strategy. *Renew. Energy*. **186**, 366-377 (2022).
7. Topham, E. & McMillan, D. Sustainable decommissioning of an offshore wind farm. *Renew. Energy*. **102**, 470-480 (2017).
8. Tanikawa, H., Fishman, T., Okuoka, K. & Sugimoto, K. The Weight of Society Over Time and Space: A Comprehensive Account of the Construction Material Stock of Japan, 1945–2010. *J. Ind. Ecol.* **19**, 778-791 (2015).
9. Geudtner, D., Torres, R., Snoeij, P., Davidson, M. & Rommen, B. Sentinel-1 system capabilities and applications. 2014 IEEE Geoscience and Remote Sensing Symposium. 2014: IEEE; 2014. p. 1457-1460.
10. Bennett, J. *OpenStreetMap*. (Packt Publishing Ltd, 2010).
11. Andreone, G. The exclusive economic zone. *Https://Www.Marineregions.Org/Downloads.Php*, (2015).
12. Danish Energy Agency. Master Data Register of Wind Turbines. *Https://Turbines.Dk/About/*, (2018).
13. The Wind Power. Wind Energy Database, The Wind Power Database. *Https://Www.Thewindpower.Net/Index.Php*, (2020).
14. Coffshore. Global Offshore Renewable Map, 4Coffshore Database. *Https://Www.4Cofshore.Com/Ofshorewind/*, (2020).
15. Wind-turbine-models. Database of wind turbines. *Https://Doi.Org/Https://En.Wind-Turbine-Models.Com/*, (2019).
16. Zhang, T., Tian, B., Sengupta, D., Zhang, L. & Si, Y. Global offshore wind turbine dataset. *Sci. Data*. **8**, 191 (2021).
17. Xu, W. et al. Proliferation of offshore wind farms in the North Sea and surrounding waters revealed by satellite image time series. *Renewable and Sustainable Energy Reviews*. **133**, 110167 (2020).
18. Hoeser, T. & Kuenzer, C. SyntEO: Synthetic dataset generation for earth observation and deep learning–Demonstrated for offshore wind farm detection. *Isprs-J. Photogramm. Remote Sens.* **189**, 163-184 (2022).
19. Lopez-Olocco, T. et al. Experimental comparison of a dual-spar floating wind farm with shared mooring against a single floating wind turbine under wave conditions. *Eng. Struct.* **292**, 116475

(2023).

20. Cai, W., Hu, Y., Fang, F., Yao, L. & Liu, J. Wind farm power production and fatigue load optimization based on dynamic partitioning and wake redirection of wind turbines. *Appl. Energy*. **339**, 121000 (2023).
21. Bai, X., Xie, Z., Xu, X. & Xiao, Y. An adaptive threshold fast DBSCAN algorithm with preserved trajectory feature points for vessel trajectory clustering. *Ocean Eng.* **280**, 114930 (2023).
22. Gorelick, N. Google earth engine. EGU general assembly conference abstracts. 2013: American Geophysical Union Vienna, Austria; 2013. p. 11997.
23. Zhang, T., Tian, B., Sengupta, D., Zhang, L. & Si, Y. Global offshore wind turbine dataset. *Sci. Data*. **8**, (2021).
24. Chang, K. & Jeng, D. Numerical study for wave-induced seabed response around offshore wind turbine foundation in Donghai offshore wind farm, Shanghai, China. *Ocean Eng.* **85**, 32-43 (2014).
25. Xu, Z. et al. Dynamic detection of offshore wind turbines by spatial machine learning from spaceborne synthetic aperture radar imagery. *Journal of King Saud University - Computer and Information Sciences*. **34**, 1674-1686 (2022).
26. Huang, X., Ma, T., Liu, C. & Liu, S. GriT-DBSCAN: A spatial clustering algorithm for very large databases. *Pattern Recognit.* **142**, 109658 (2023).
27. Chen, Z., Kleijn, R. & Lin, H. X. Metal requirements for building electrical grid systems of global wind power and utility-scale solar photovoltaic until 2050. *Environ. Sci. Technol.* **57**, 1080-1091 (2022).
28. Cai, R., Zhang, L., Cheng, M., Yang, X. & Ren, D. Research on the technical and economic performance of 66 kV offshore wind power AC power collection scheme. *Journal of Global Energy Interconnection*. **2**, (2019).
29. Li, J. et al. Critical rare-earth elements mismatch global wind-power ambitions. *One Earth*. **3**, 116-125 (2020).
30. Zhang, J. & Wang, H. Development of offshore wind power and foundation technology for offshore wind turbines in China. *Ocean Eng.* **266**, 113256 (2022).
31. Council, G. W. E. Global offshore wind report 2020. *Gwec: Brussels, Belgium*. **19**, 10-12 (2020).
32. Li, M. Overview of China's submarine cable industry., (2022).
33. Xie, W. Commodities in the context of wind power development. *Https://Pdf.Dfcfw.Com/Pdf/H3_Ap202306021588386857_1.Pdf?1685713661000.Pdf*, (2023).